nature biomedical engineering

ARTICLES

https://doi.org/10.1038/s41551-019-0416-1

PET imaging of occult tumours by temporal integration of tumour-acidosis signals from pH-sensitive ^{64}Cu-labelled polymers

Gang Huang[1], Tian Zhao[1], Chensu Wang[1], Kien Nham[2], Yahong Xiong[2], Xiaofei Gao[3], Yihui Wang[3], Guiyang Hao[2], Woo-Ping Ge[3], Xiankai Sun[2], Baran D. Sumer[4*] and Jinming Gao[1,4*]

Owing to the diversity of cancer types and the spatiotemporal heterogeneity of tumour signals, high-resolution imaging of occult malignancy is challenging. ^{18}F-fluorodeoxyglucose positron emission tomography allows for near-universal cancer detection, yet in many clinical scenarios it is hampered by false positives. Here, we report a method for the amplification of imaging contrast in tumours via the temporal integration of the imaging signals triggered by tumour acidosis. This method exploits the catastrophic disassembly, at the acidic pH of the tumour milieu, of pH-sensitive positron-emitting neutral copolymer micelles into polycationic polymers, which are then internalized and retained by the cancer cells. Positron emission tomography imaging of the ^{64}Cu-labelled polymers detected small occult tumours (10–20 mm^3) in the brain, head, neck and breast of mice at much higher contrast than ^{18}F-fluorodeoxyglucose, ^{11}C-methionine and pH-insensitive ^{64}Cu-labelled nanoparticles. We also show that the pH-sensitive probes reduce false positive detection rates in a mouse model of non-cancerous lipopolysaccharide-induced inflammation. This macromolecular strategy for integrating tumour acidosis should enable improved cancer detection, surveillance and staging.

Cancer exhibits diverse genetic and histological differences from normal tissues[1]. Molecular characterization of these differences is useful to stratify patients towards personalized therapy. However, the strategy may not serve as a broad diagnostic tool because genetic/phenotypic biomarkers are expressed in a subset of patients, and significant overlap with normal tissues exists[2,3]. Deregulated energetics are hallmarks of cancer that occur across many types of cancer[4]. Elevated glucose metabolism in cancer cells has long been associated with aerobic glycolysis, where cancer cells preferentially take up glucose and convert it into lactic acid[5]. More recent studies using ^{13}C-labelled glucose in lung cancer patients further show accelerated oxidative phosphorylation in addition to glycolysis as a cancer cell mechanism for growth and proliferation[6]. The clinical significance of the glucose metabolism is manifested by the widespread use of ^{18}F-fluorodeoxyglucose (FDG) positron emission tomography (PET)[7], where FDG—a radiolabelled glucose analogue—is selectively taken up by overexpressed glucose transporters and trapped inside the cancer cells after phosphorylation by hexokinase for PET detection[8].

Despite broad clinical adoption, FDG has many well-described pitfalls[9–16], including relatively high false rates, depending on tumour size and variable levels of FDG uptake in tumours and normal tissues. High physiological uptake of FDG typically occurs in the brain, heart, kidneys and urinary tract, obscuring the tumour signal from areas adjacent to these tissues[11]. In head and neck cancer, high FDG uptake in the Waldeyer's ring (nasopharyngeal, palatine and lingual tonsils), salivary glands, striated muscle or brown fat, and inflammation/infection all contribute to false positive signals[17,18]. For tumours <1 cm, inadequate accumulation of FDG in tumours over the surrounding normal tissues often leads to false negatives[9,10,15,19]. In addition, skull base tumours in the vicinity of highly metabolic brain parenchyma or oropharyngeal and nasopharyngeal cancers in FDG-avid tonsillar tissue, may yield false negative diagnoses[20–23]. The variability of FDG uptake, overlap in retention, and temporal fluctuations in metabolism for both normal and tumour tissues significantly limit the accuracy of FDG-PET in cancer detection.

Previously, we reported an indocyanine green (ICG)-encoded ultra-pH-sensitive (UPS) nanoprobe for the broad detection of a wide range of solid cancers by near-infrared fluorescence imaging[24]. This optical tracer exploits the phase transition of the polymers to quench and unquench the fluorescence of dyes conjugated to the hydrophobic portion of the polymers. The optical output is discrete (all on or off with no intermediate values), leading to the high specificity and sensitivity in tumour detection. However, it was unclear whether the phase transition behaviour of the polymers could be harnessed to generate a response or output other than fluorescence. In the tumour milieu, irreversible capture and integration of polycationic unimers on pH activation of neutral circulating micelles can lead to an increase in the polymer dose in acidotic tumours over the surrounding normal tissues. Based on this insight, we hypothesized that the catastrophic phase transition responsible for the binary fluorescence response could be further exploited to achieve binary tumour-specific tissue retention or capture of the activated nanoprobes. Temporal integration of this activated and captured signal can provide signal amplification in only tumours, to overcome the spatiotemporal limitations of FDG. To test this hypothesis, we synthesized a positron-emitting radionuclide (^{64}Cu; $t_{1/2}$ = 12.7 h)-encoded

[1]Harold C. Simmons Comprehensive Cancer Center, University of Texas Southwestern Medical Center, Dallas, TX, USA. [2]Department of Radiology, University of Texas Southwestern Medical Center, Dallas, TX, USA. [3]Children's Research Institute, Departments of Pediatrics, Neuroscience, and Neurology and Neurotherapeutics, University of Texas Southwestern Medical Center, Dallas, TX, USA. [4]Department of Otolaryngology, University of Texas Southwestern Medical Center, Dallas, Texas, USA. *e-mail: baran.sumer@utsouthwestern.edu; jinming.gao@utsouthwestern.edu

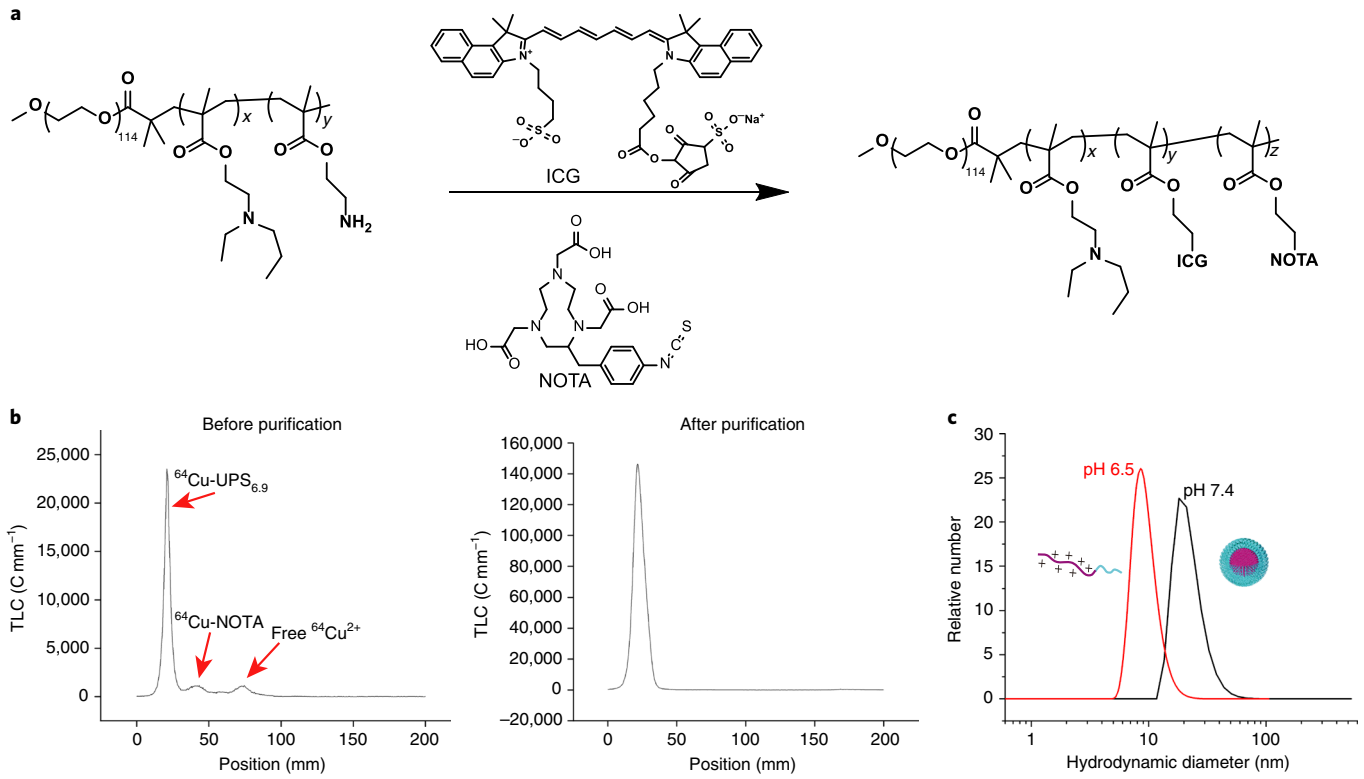

Fig. 1 | Synthesis and characterization of ^{64}Cu-UPS$_{6.9}$ nanoprobes. a, Schematic of the syntheses of NOTA- and ICG-conjugated PEG-*b*-PEPA block copolymers. **b**, Radio-TLC chromatogram of ^{64}Cu-UPS$_{6.9}$ nanoprobes before (left) and after centrifugation purification (right). The labelling efficiency was measured with saline as the developing eluent, and was shown to be more than 95%. **c**, Dynamic light scattering analysis of UPS$_{6.9}$ nanoprobes at pH 7.4 and 6.5 (above and below the pH transition threshold, respectively).

UPS nanosensor with dual PET and fluorescence functions. PET imaging using ^{64}Cu-UPS showed clear detection of occult malignancy in the brain, head and neck, and breast over conventional FDG. Capture of polymers within tumours on activation represents a second output (in addition to fluorescence) that can be exploited for non-invasive imaging of cancer nodules by PET.

Results

Synthesis of the ^{64}Cu-UPS$_{6.9}$ nanosensor. 1,4,7-triazacyclononane-*N*,*N*′,*N*″-trisacetic acid (NOTA)- and ICG-conjugated poly(ethylene glycol)-*b*-poly(ethylpropylaminoethyl methacrylate) (PEG-*b*-PEPA) copolymer (also known as UPS$_{6.9}$ for pH transition at 6.9) was synthesized via the atom transfer radical polymerization method (Fig. 1a)[25]. The average numbers of NOTA and ICG per copolymer were determined to be two and one, respectively. After polymer synthesis, ^{64}Cu chelation to NOTA was carried out at 37 °C and pH 6.5 for 15 min to ensure fully dissociated unimers for efficient copper binding (95%; Fig. 1b). After ^{64}Cu labelling, the solution was brought back to pH 7.4 in sodium carbonate buffer to form micelle nanoparticles (32.7 ± 1.6 nm) (Fig. 1c). Removal of unbound ^{64}CuCl$_2$ and the ^{64}Cu-NOTA complex was achieved by centrifugal membrane filtration three times with a molecular weight cutoff of 100 kD. The specific activity of the ^{64}Cu-UPS nanosensor is 5.5 mCi mg^{-1} (per mass unit) or 165 Ci mmol^{-1} for molar activity (~6% NOTA on the UPS polymers were labelled with ^{64}Cu to match the optimum dose for fluorescence imaging). The resulting ^{64}Cu-UPS nanosensor was stable in the mouse serum within 48 h, as determined by radio thin-layer chromatography (TLC) and fluorescence assays (Supplementary Fig. 1). Lowering the pH below the transition pH (6.9) led to micelle dissociation into unimers (8.4 ± 0.2 nm). For comparison, NOTA-conjugated poly(ethylene glycol)-*b*-poly(D,L-lactic acid) (PEG-PLA) nanoparticles of a similar size (32.0 ± 2.4 nm) were also synthesized as a non-pH-sensitive nanosensor control (Supplementary Fig. 2).

Irreversible activation of ^{64}Cu-UPS$_{6.9}$ in biological milieu. In aqueous saline solution (protein free), UPS$_{6.9}$ copolymers undergo 'reversible' micelle assembly/disassembly across a narrow pH span (<0.2 pH; Fig. 2a,b). The protonation process is highly cooperative with a Hill coefficient of 38 (Fig. 2c). Along the pH titration coordinate, nanophase segregation (that is, micellization) rendered a bistable-state solution consisting of highly protonated unimers in solution versus neutral copolymers in micelles (Fig. 2d). This all-or-nothing protonation phenotype without the intermediate states is a hallmark of positive cooperativity[26,27]. The divergent physical properties of the neutral PEGylated micelles and polycationic unimers account for the molecular basis of capture and integration mechanism in the biological system.

In biological milieu, serum protein binding can 'irreversibly' arrest UPS copolymers in the dissociated unimer state on pH activation of PEGylated micelles (Fig. 3a). We examined the reversibility of the UPS$_{6.9}$ nanoprobes in the presence or absence of 40 mg ml^{-1} human serum albumin (HSA) (Fig. 3b). The results show that in the absence of HSA, UPS$_{6.9}$ fluorescence intensity returned to the base level after the pH was reversed from 6.5 to 7.4 multiple times. In contrast, in the presence of HSA, the fluorescence intensity was kept at the 'on' state after pH reversal. These data suggest that the nanoprobe response can be drastically different in the biological environment compared with pristine buffer solutions. This irreversible characteristic contributes to the capture of persistent but fluctuating tumour acidotic signals into stabilized output.

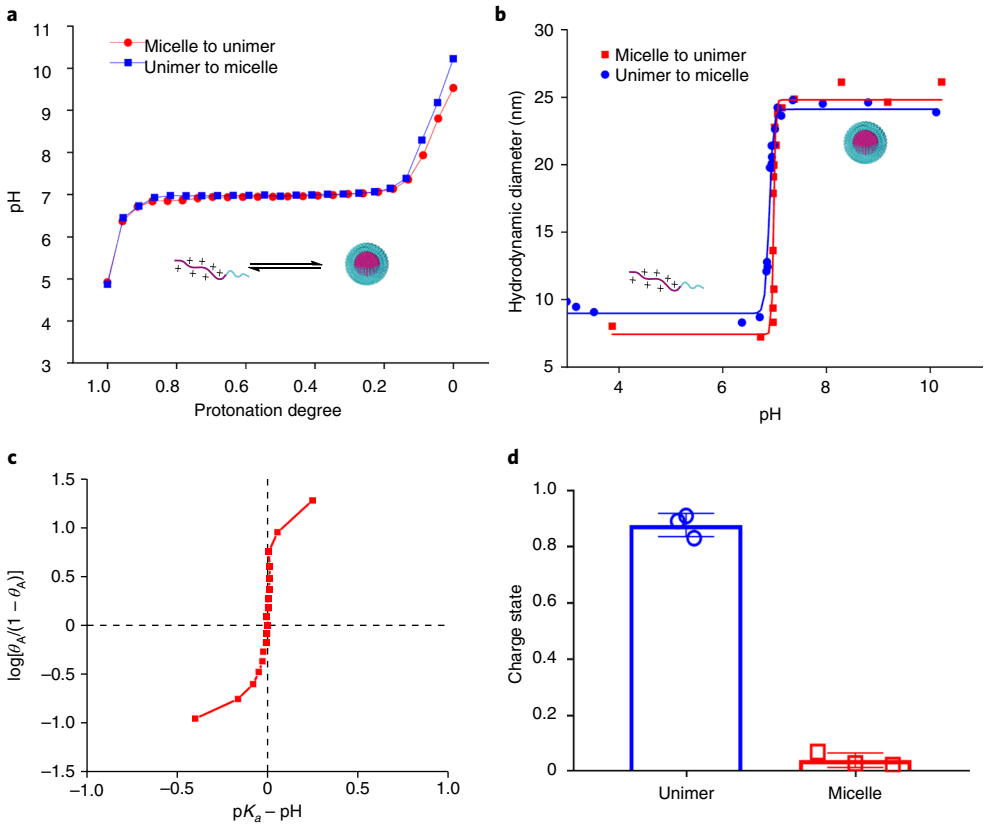

Fig. 2 | All-or-nothing proton distribution of $UPS_{6.9}$ nanoprobes. a, pH titration curve of $UPS_{6.9}$, showing a reversible and sharp pH transition in saline solution. **b**, Reversible hydrodynamic size change of $UPS_{6.9}$ along the pH titration coordinate. **c**, Quantification of proton binding cooperativity by the UPS copolymers yields a Hill coefficient of 38. The Hill plot is used to evaluate the strength of cooperativity by plotting $\log(\theta_A/(1-\theta_A))$ versus (pKa − pH), where θ_A is the protonation degree. **d**, Quantification of unimer and micelle charge states of $UPS_{6.9}$ at an overall protonation degree of 50%. Protons were distributed divergently where unimers were highly charged (~90%) and micelles were almost neutral. Individual data points are shown. Bar heights and error bars represent means ± s.d. ($n = 3$).

Irreversible capture and uptake of ^{64}Cu-$UPS_{6.9}$. To investigate whether acidic pH can impact nanoprobe uptake inside cancer cells, we incubated ^{64}Cu-$UPS_{6.9}$ with HN5 head and neck cancer cells in DMEM medium at pH 6.5 and 7.4. To mimic the physiological environment, 40 mg ml^{-1} HSA was added to the medium. For comparison, ^{64}Cu-PEG-PLA nanoparticles were used as a non-pH-sensitive control. HN5 cells were incubated with the same dose of either nanoparticle (25 μg ml^{-1}) for different time periods. Then, the radioactive medium was replaced and washed with medium without the tracers. Autoradiography images of HN5 cells from the 96-well plate show pH-dependent uptake of ^{64}Cu-$UPS_{6.9}$. At pH 6.5, increased amounts of positron signals were detected over time, leading to an approximately fivefold increase in cell uptake at 1 h over that at pH 7.4 (Fig. 3c,d and Supplementary Figs. 3 and 4). Albumin-mediated unimer uptake was investigated by pretreating UPS nanoprobes at pH 6.5 in the presence of HSA. The pH was then brought back to 7.4. It was found that 50% of polymer uptake occurred in HN5 cells at pH 6.5 (Supplementary Fig. 5). HN5 cells incubated with non-pH-sensitive ^{64}Cu-PEG-PLA micelles did not show any observable pH dependence in radioactivity signals, and the cell uptake remained low at both pH levels, consistent with the stealth properties of PEGylated micelle nanoparticles[28]. We used laser confocal scanning microscopy to examine the distribution of the $UPS_{6.9}$ (free of ^{64}Cu to avoid radiation exposure) 5 and 60 min after incubation in albumin-containing medium at pH 6.5. HN5 cells were stained for nucleus, cell membrane and lysosomes with Hoechst (blue), anti-F-actin (cyan) and anti-lysosomal-associated membrane protein 1 (green), respectively. Anti-poly(ethylene glycol) antibody was used to label the $UPS_{6.9}$ copolymer. Data show the initial adhesion of the copolymer on the cell surface, followed by internalization inside the HN5 cells at 60 min. An image overlay shows the internalized $UPS_{6.9}$ punctates colocalized with lysosomes (Fig. 3e).

Capture and integration of ^{64}Cu-$UPS_{6.9}$ in the HN5 tumours. Spatiotemporal characterization of ^{64}Cu-$UPS_{6.9}$ distribution in orthotopic HN5 tumours in vivo further validated the capture and integration mechanism. HN5 cancer cells were inoculated in the submental space in the head and neck area of a severe combined immunodeficient mouse. After tumours grew to 100–200 mm^3, ^{64}Cu-$UPS_{6.9}$ tracer (0.1 mCi) was injected through the tail vein. At 30 min, 3 h and 24 h, animals were sacrificed and tumours were removed and resected into 30-μm-thin slices. Autoradiography analysis showed the initial sporadic capture of ^{64}Cu-$UPS_{6.9}$ in HN5 tumours (mostly at the tumour periphery) at 30 min and 3 h, as verified by haematoxylin and eosin histology, followed by increased tracer accumulation throughout the whole tumour at 24 h (Supplementary Fig. 6).

^{64}Cu-$UPS_{6.9}$ reduced false detection of inflammation by FDG. Non-cancerous tissue inflammation (for example, infection) frequently causes false positive FDG-PET results because inflammatory cells use glucose as a primary source of energy[29]. To compare the imaging response to tissue inflammation by ^{64}Cu-$UPS_{6.9}$ versus FDG, we employed a lipopolysaccharide (LPS)-induced, tumour-free animal model for evaluation. In these experiments, healthy BALB/c mice were used. Two days before PET imaging, LPS was

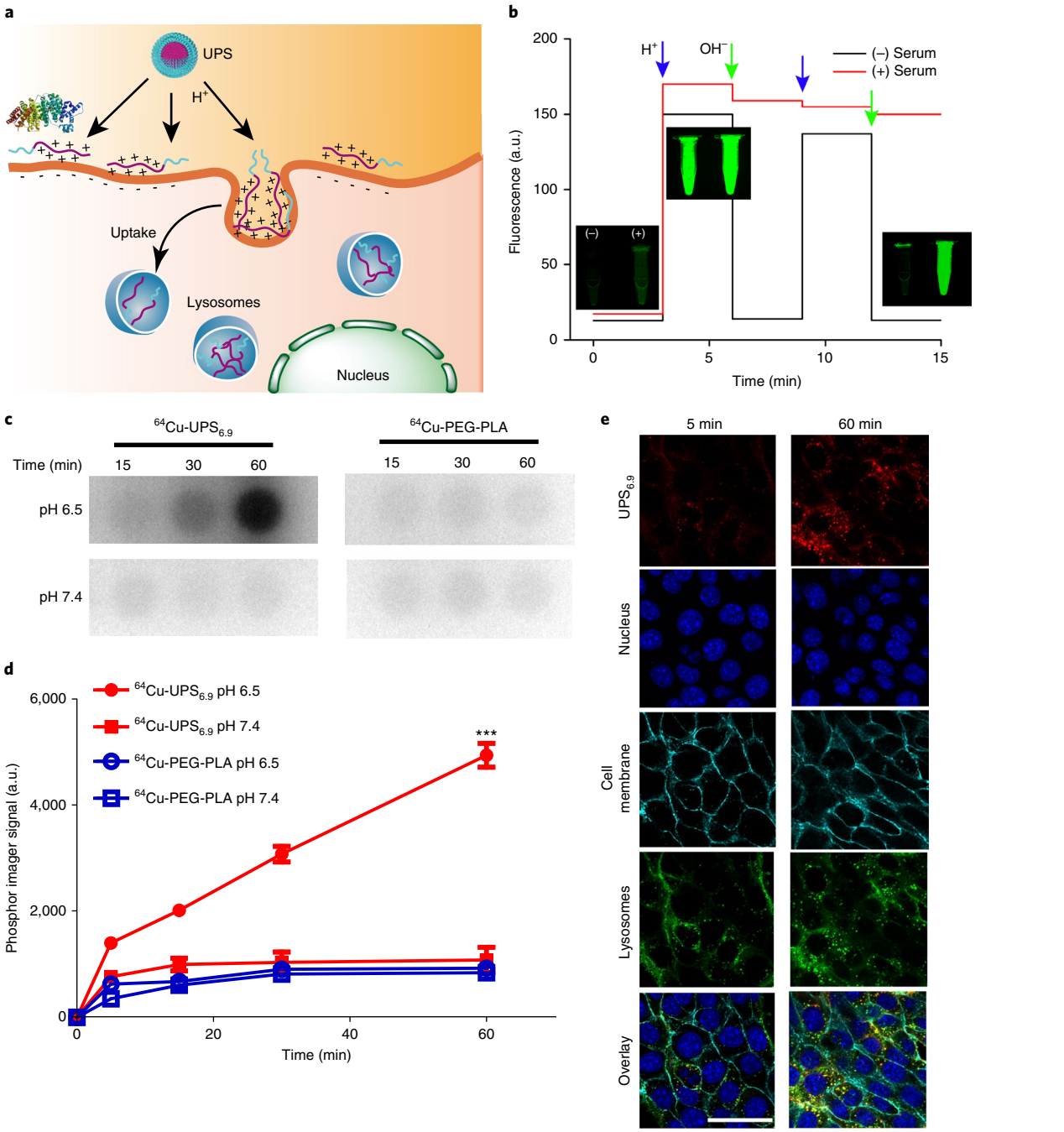

Fig. 3 | Irreversible capture of UPS nanoprobes by serum protein binding and cancer cell uptake after pH activation. a, Schematic of acid-activated protein binding and membrane adhesion of UPS tracers, leading to their sequestration inside lysosomes of cancer cells. **b**, Irreversible arrest of UPS tracers in the unimer state in the presence of serum proteins, even after pH reversal to 7.4, compared with the reversible fluorescence changes in the absence of serum proteins. **c**, Autoradiography images of HN5 cells incubated with ^{64}Cu-UPS$_{6.9}$ and ^{64}Cu-PEG-PLA nanoparticles (both at 25 μg ml^{-1}) at pH 6.5 and 7.4 over time. **d**, Significantly higher cell uptake of UPS$_{6.9}$ was found at pH 6.5 compared with pH 7.4, and compared with ^{64}Cu-PEG-PLA tracers at both pH levels. Data are presented as means ± s.d ($n = 3$). Statistical significance (***$P = 0.0003$) was determined by unpaired two-sided Student's *t*-test, compared with other groups. **e**, Confocal microscopy showed that UPS$_{6.9}$ was mostly bound to cell membranes at 5 min, followed by lysosome colocalization at 60 min after incubation with HN5 cells. Scale bar, 50 μm.

injected subcutaneously into the right hind leg of mice to induce inflammation, while phosphate buffered saline (PBS) was injected into the left hind leg as a control. FDG (150 μCi) and ^{64}Cu-UPS$_{6.9}$ (120 μCi) were intravenously injected and imaged 1 and 24 h postinjection, respectively. The FDG signal was significantly higher at the inflammation site (3.4 ± 0.2% of the injected dose per gram of tissue (%ID g^{-1}) compared with the normal muscle tissue (0.7 ± 0.2%ID g^{-1}; ($P < 0.01$; Fig. 4 and Supplementary Fig. 7). In contrast, ^{64}Cu-UPS$_{6.9}$ showed a slightly increased signal at the LPS injection site (0.56 ± 0.13%ID g^{-1}) over the control muscle tissue (0.32 ± 0.05%ID g^{-1}), but this difference was not statistically significant. The contrast ratios of inflammation tissue over normal tissue were 4.9 ± 1.3 for FDG and 1.7 ± 0.5 for ^{64}Cu-UPS$_{6.9}$. The lower contrast ratio by ^{64}Cu-UPS$_{6.9}$ offers a potential advantage via the

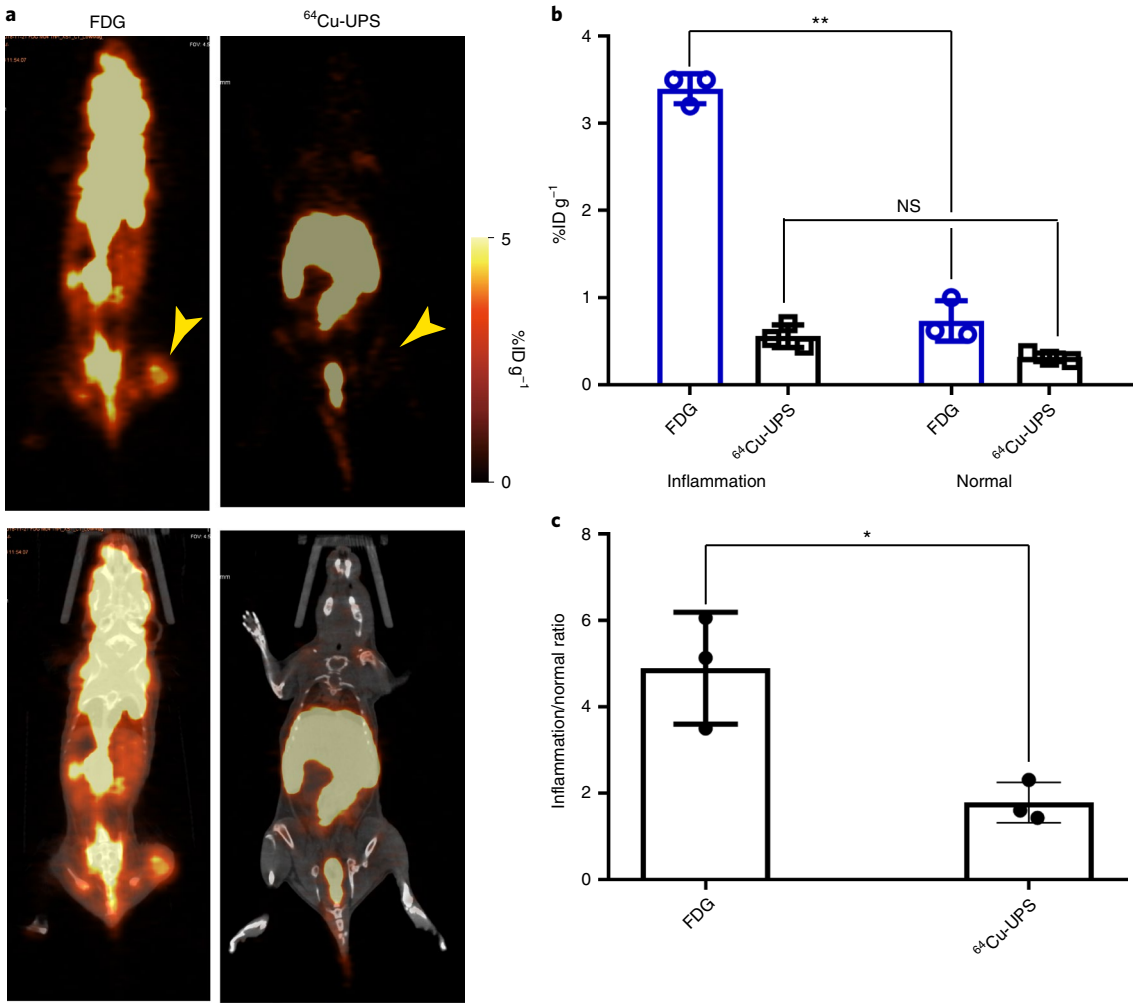

Fig. 4 | ^{64}Cu-UPS$_{6.9}$ reduced false positive PET signals from LPS-induced inflammation compared with FDG. a, PET/computed tomography imaging of BALB/c mice with LPS injection in the right hind legs, by FDG (left) and ^{64}Cu-UPS$_{6.9}$ (right). Arrow heads point to the LPS injection sites in the muscle tissues. Top: PET images; Bottom: Fused PET/computed tomography images. Representative images are shown ($n=3$). **b**, Quantification of PET signals from the inflammation sites and normal left leg muscle tissues by FDG and ^{64}Cu-UPS$_{6.9}$. Significance (**$P=0.0024$) was determined by paired two-sided Student's t-test. NS, not significant. **c**, Inflammation-tissue-to-normal-muscle ratios by PET, for ^{64}Cu-UPS$_{6.9}$ and FDG. Significance (*$P=0.017$) was determined by unpaired two-sided Student's t-test. In **b** and **c**, individual data points are shown. Bar heights and error bars represent means ± s.d. ($n=3$).

reduction of false positive signals from tissue inflammation normally observed in FDG-PET.

^{64}Cu-UPS$_{6.9}$ achieved binary detection of brain tumours. Brain cancer is one of the most lethal forms of cancer without a widely accepted method for early detection[30]. Late diagnosis when symptoms occur often leads to poor prognosis and survival[31]. Conventional metabolic PET tracer FDG cannot be used for brain tumour imaging because of the high physiological uptake of glucose in the normal brain tissues[32]. To investigate the feasibility of ^{64}Cu-UPS$_{6.9}$ for glioma detection, we utilized an orthotopic glioma mouse model by transplantation of a green fluorescent protein (GFP)-labelled murine glioma cell line, 73C (astrocyte-derived gliomas with *p53*$^{-/-}$, *PTEN*$^{-/-}$ and *BRAF*^{V600E} mutations), into the stratum of mouse brains. At 24 h after intravenous administration of ^{64}Cu-UPS$_{6.9}$, PET imaging showed bright illumination of small-sized brain tumours (~10 mm^3) over the dark normal brain tissue background (Fig. 5a and Supplementary Fig. 8). Tissue uptake of ^{64}Cu-UPS$_{6.9}$ was measured at 3.1 ± 1.6 and 0.54 ± 0.3%ID g^{-1} for 73C tumours and normal brain tissues, respectively. The contrast-to-noise ratio (CNR) was determined to be 15.1 ± 6.8, and the tumour-to-background ratio (TBR) was 6.0 ± 1.6. For comparison, ^{11}C-methionine (MET)—a newly developed amino acid tracer for brain tumour imaging[33–35]—was also employed to detect 73C tumours. After intravenous administration, the tissue uptake of MET in tumours was 3.1 ± 0.4%ID g^{-1} at 20 min. Normal brain tissues had relatively high uptake of MET at 1.9 ± 0.2%ID g^{-1}, lowering the CNR to 2.8 ± 0.7 and the TBR to 1.6 ± 0.1 compared with ^{64}Cu-UPS$_{6.9}$ (Supplementary Fig. 9). In the normal brain tissues, the blood–brain barrier was effective at keeping the PEGylated micelle form of ^{64}Cu-UPS$_{6.9}$ out of the brain parenchyma. In 73C gliomas, tumour acidosis was able to activate ^{64}Cu-UPS$_{6.9}$, leading to significantly increased positron signals. Subsequent investigation of brain tumour slides (8 µm in thickness) by autoradiography and ICG fluorescence correlated microscopically with haematoxylin and eosin histology and GFP fluorescence (Fig. 5b). Fluorescence microscopy data further illustrate that the UPS tracer can cross the blood tumour barrier in 73C gliomas and not only accumulate at the perivascular area, but also distribute broadly in the tumour sections (overlay image in Fig. 5c and Supplementary Fig. 10). These data corroborate the feasibility of irreversibly trapping UPS tracers in brain cancer cells

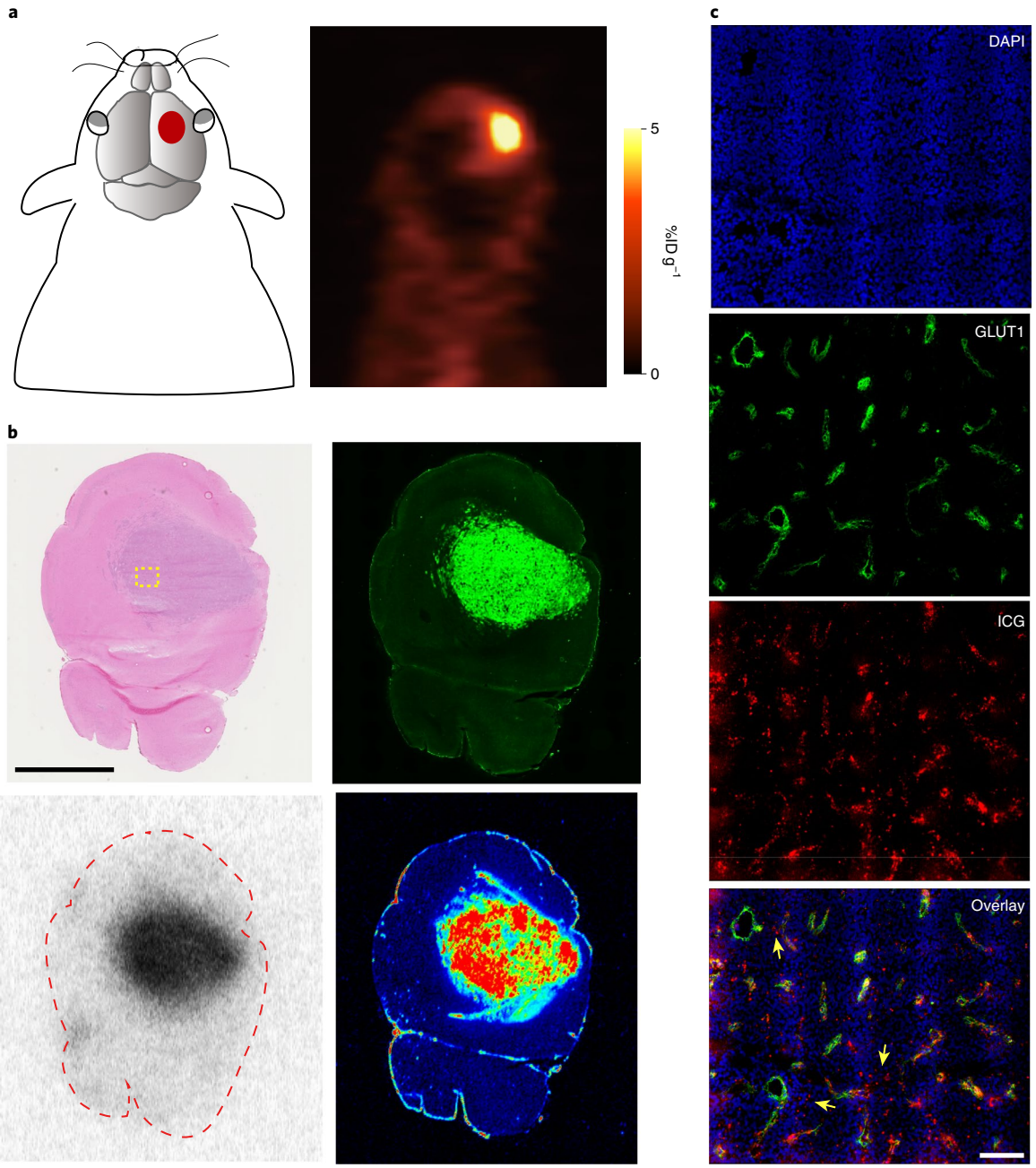

Fig. 5 | The 'capture and integration' strategy allowed binary detection of a brain tumour at both macroscopic (animal) and microscopic (subcellular) levels. a, PET imaging of an orthotopic 73C murine brain tumour in a C57BL/6 mouse by ^{64}Cu-UPS$_{6.9}$. **b**, Correlation of haematoxylin and eosin (top left), GFP fluorescence (top right), autoradiography (bottom left) and ICG fluorescence imaging (bottom right) of a brain tumour slide supports the cancer-specific imaging by UPS nanoprobes. Scale bar, 2.5 mm. **c**, Fluorescence microscopy analysis of UPS tracer in brain tumours. Correlation of the ICG and glucose transporter 1 (GLUT1) signals showed that UPS nanoprobes are not only located at the perivascular sites, but also distributed throughout the tumours. 4′,6-diamidino-2-phenylindole (DAPI) shows the nucleus, GLUT1 the vasculature and ICG the UPS nanoprobes. Yellow arrows point to the UPS nanoprobes away from the vasculature. Scale bar, 100 μm. Representative images are shown ($n = 4$).

to achieve binary tumour imaging outcomes at both macroscopic and microscopic levels.

Non-invasive imaging of multiple tumour types by ^{64}Cu-UPS$_{6.9}$. To investigate the feasibility of ^{64}Cu-UPS$_{6.9}$ to image a broad set of cancers, we evaluated PET imaging of additional head/neck and breast tumour nodules. ^{64}Cu-UPS$_{6.9}$ tracers (0.1 mCi) were injected into the tail vein of tumour-bearing mice. The results show conspicuous detection of occult nodules (10–20 mm^3) in orthotopic HN5 and FaDu head and neck tumours, as well as 4T1 triple-negative breast tumours (Fig. 6a and Supplementary Figs. 9–11 for triplicate reports showing the robustness of tumour detection). Autoradiography images on another set of tumour models with tumour invasion to the surrounding muscles also showed increased accumulation of ^{64}Cu-UPS in the tumour tissues over the surrounding normal muscles (Supplementary Fig. 11–13). The tissue uptakes were 9.9 ± 2.5, 6.5 ± 2.5 and 5.7 ± 1.2%ID g^{-1} in the HN5, FaDu and 4T1 tumours 18–24 h after intravenous injection of ^{64}Cu-UPS$_{6.9}$ tracers, respectively. The CNRs were 54.3 ± 8.7, 33.5 ± 3.7 and 34.6 ± 12.1 in the HN5, FaDu and 4T1 tumours ($n = 3$ for each tumour type),

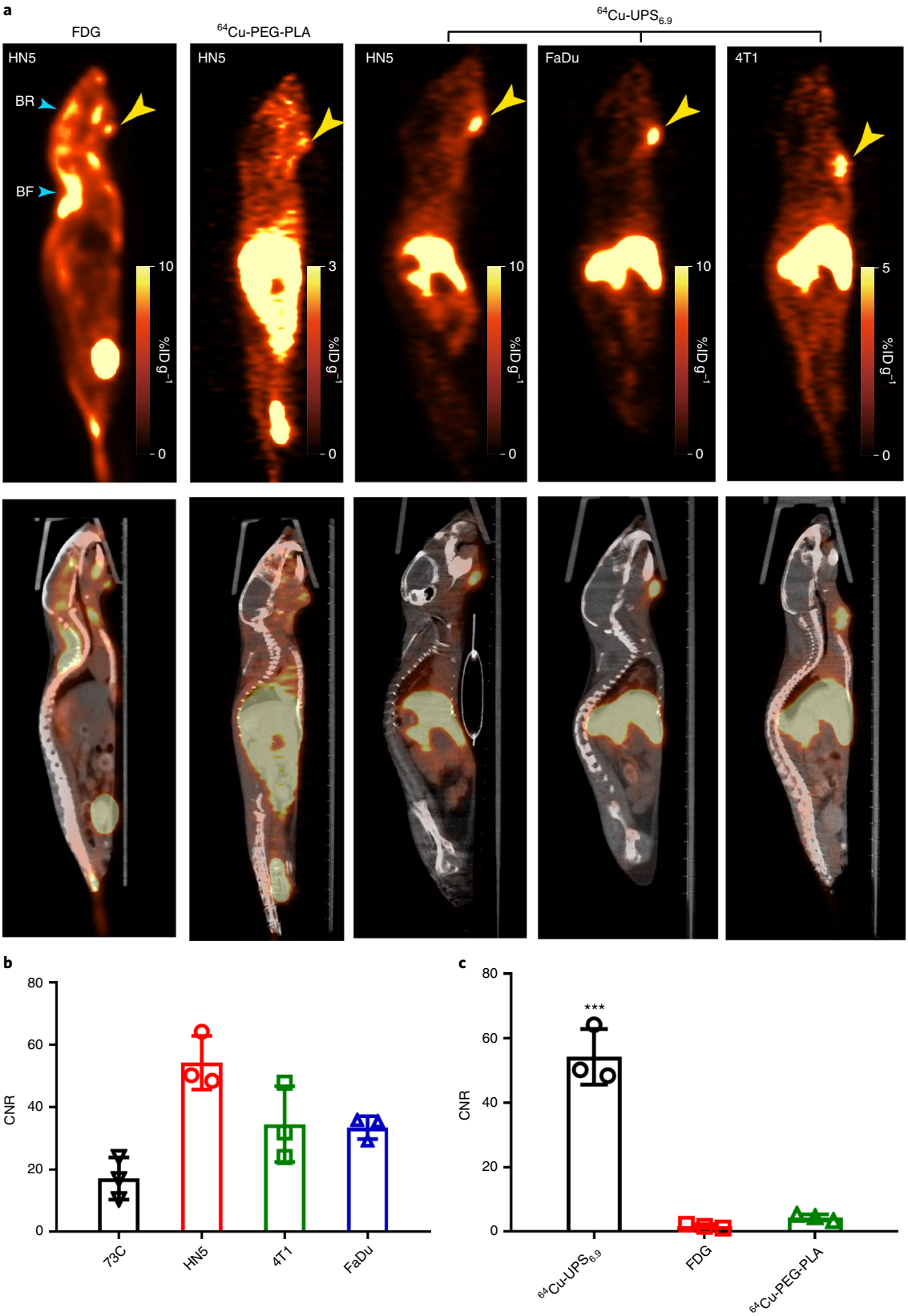

Fig. 6 | Non-invasive digitization of tumour acidotic signals by PET. a, Cancer-specific detection of various small tumour nodules (10–20 mm^3) by intravenously administered ^{64}Cu-UPS tracers. Orthotopic HN5 and FdDu head and neck cancers, and 4T1 triple-negative breast cancer were clearly visualized. Top: PET images; Bottom: Fused PET/computed tomography images. Yellow arrow heads point to the tumour site. Representative images are shown ($n=3$). The liver and spleen are the other major organs for UPS uptake. FDG-PET imaging showed high false rates in the head and neck region. BF, brown fat; BR, brain. **b**, PET quantification of CNR values for ^{64}Cu-$UPS_{6.9}$ in different tumour models. **c**, Comparison of CNR values in HN5 tumours by ^{64}Cu-$UPS_{6.9}$ versus FDG and ^{64}Cu-PEG-PLA nanoparticles. Significance (***$P=0.0006$) was determined by unpaired two-sided Student's *t*-test. In **b** and **c**, individual data points are shown. Bar heights and error bars represent means ± s.d ($n=3$).

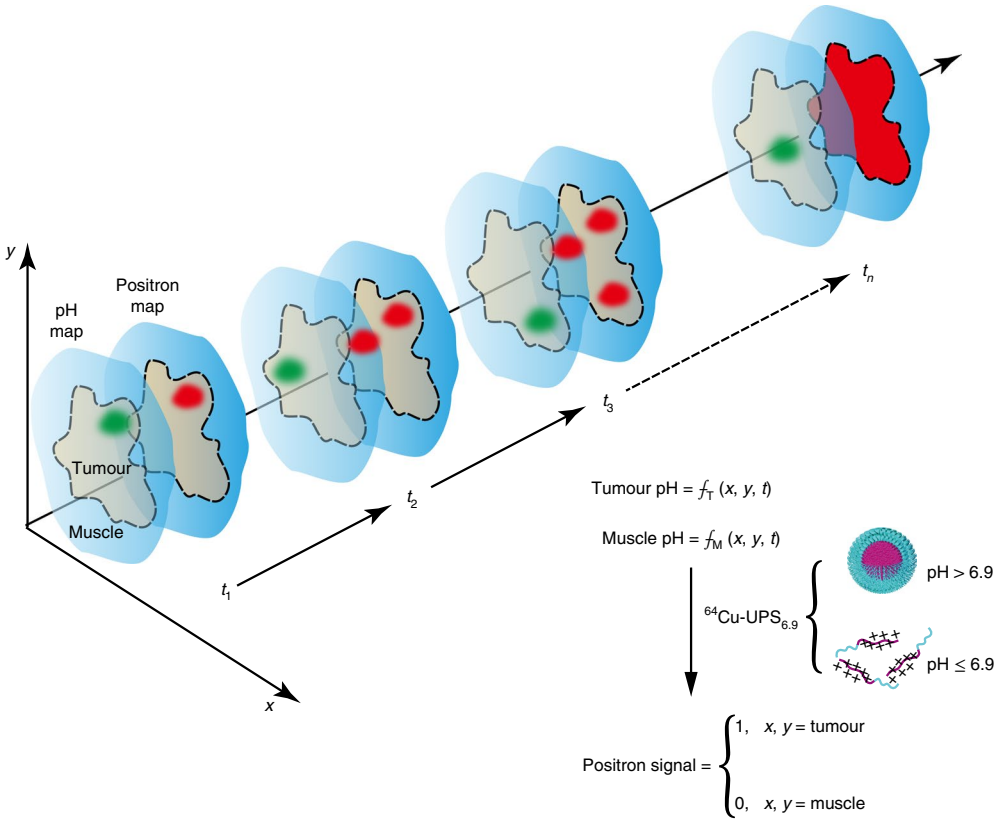

Fig. 7 | Schematic of the capture and integration algorithm. Perpetual spatiotemporal fluctuations in tumour acidosis are converted into step functions of binary response (0 and 1) by the proton transistor sensor. At specific times (t_1, t_2…t_n), different regions of the tumour are acidified below the pH threshold (6.9), as indicated by the green spots. The acidic pH signal is permanently captured by ^{64}Cu-UPS$_{6.9}$, as indicated by the red spots on the positron map. Over time, integration of positron signals yields a binary tumour map over the normal muscle background. f_T and f_M represent the tissue pH as a function of space and time in the tumour and muscle, respectively.

respectively (Fig. 6b). The TBR values were 21.5 ± 5.6, 16.7 ± 6.0 and 15.6 ± 3.4 in the above three tumour models, respectively. PET imaging using FDG (0.15 mCi) and ^{64}Cu-PEG-PLA (0.12 mCi) in HN5 tumours showed less striking imaging outcomes. In FDG-PET experiments, despite HN5 tumour contrast (5.4 ± 0.7%ID g^{-1}), non-specific uptake of FDG in the brain (7.9 ± 1.6%ID g^{-1}), brown fats (8.1 ± 1.3%ID g^{-1}) and tensed muscles (6.3 ± 0.3%ID g^{-1}) created false positive signals that complicated tumour diagnosis (Fig. 6a,c and Supplementary Fig. 14). The high background noise also decreased the CNR value to 1.7 ± 0.6 and the TBR value to 2.0 ± 0.5. In the ^{64}Cu-PEG-PLA study, a small percentage (2.0 ± 0.2%ID g^{-1}) of tumour uptake was observed in HN5 tumours 18–24 h after intravenous injection. The CNR and TBR values of ^{64}Cu-PEG-PLA (4.4 ± 1.0 and 3.9 ± 0.4, respectively; Fig. 6c and Supplementary Figs. 15 and 16) were significantly lower than for ^{64}Cu-UPS$_{6.9}$ (54.3 ± 8.7 and 21.5 ± 5.6, respectively). These results show that passive targeting through the leaky tumour vasculature is not sufficient to produce high tumour contrast, as shown by the low CNR value of conventional ^{64}Cu-PEG-PLA micelle probes. To further demonstrate the effect of tumour acidosis, pretreatment of HN5 tumours with acetazolamide—an inhibitor targeting carbonic anhydrase IX (a tumour acidotic protein)—decreased the ^{64}Cu-UPS$_{6.9}$ signals by 30% compared with the PBS control (Supplementary Fig. 17).

Discussion

Biological processes are dynamic and complex, with perpetual changes in space and time. The resulting spatiotemporal heterogeneity makes it challenging to accurately diagnose pathological conditions from normal physiological background. PET or magnetic resonance imaging of acidic tumour microenvironments has been studied extensively in recent years[36–40]. However, conventional pH sensors have low pH resolution (that is, tenfold signal changes occur over 2 pH units[38–41]). Previously, we reported an ICG-based UPS nanoprobe for cancer detection by fluorescence imaging[24]. A binary fluorescent delineation of tumour margins was achieved, which led to accurate cancer surgery and prolonged survival in tumour-bearing mice. The main mechanism was thought to be the coupling of the pH-dependent phase transition phenomenon to the quenching and unquenching of the fluorophores conjugated to the hydrophobic segment of the polymers. In this study, we incorporated a ^{64}Cu PET functional moiety in the fluorescent nanoparticle formulation. Unlike the on/off fluorescence reporter, the positron signals are always 'on' and cannot be quenched; therefore, phase transition-based changes in signal analogous to fluorescence were not expected. Contrary to expectation, the positron signal showed a binary pattern of background signal suppression and tumour activation similar to the fluorescence output (Figs. 5 and 6). While PET imaging overcomes the light penetration limitations of optical imaging, we were curious about the mechanisms for the unpredicted pattern of the positron signal. Clearly, passive accumulation due to EPR effect alone was not sufficient to produce the high tumour contrast, as indicated by the relatively low CNR and TBR values of ^{64}Cu-PEG-PLA compared with ^{64}Cu-UPS in HN5 tumours.

We attribute the dramatically improved sensitivity and specificity of cancer detection by ^{64}Cu-UPS tracers to a 'capture and integration' mechanism in the acidotic tumour milieu (Fig. 7). Like most biological signals, tumour acidosis is dynamic, with high

intratumoral heterogeneity in space and time. Reversible small molecular pH sensors[42,43] do not show high tumour contrast due to broad pH responses leading to background activation and incomplete tumour activation. In addition, their signal output varies with the transient fluctuations in tumour metabolism and pH. Other pH tracers, such as the pH (low) insertion peptide (pHLIP), have been reported to undergo a similar capture mechanism by protonation and insertion into the cell membrane in the lower pH environment. However, broad pH responses and strong binding and insertion into blood cells increased background signals with reduced tumour contrast[40]. Consequently, the tumour-to-muscle ratio is around 8 by pHLIP tracers in LNCaP and PC-3 tumours at 24 h postinjection[38], compared with >30-fold for HN5 tumours by ^{64}Cu-UPS (Supplementary Table 1). For UPS nanoprobes, binary and irreversible activation below a threshold pH (for example, 6.9; readily achievable by a diverse set of tumours[44]) can permanently convert the spatiotemporal fluctuations of tumour acidotic signals into stable positron output. The sharpness of the phase transition response in this instance resulted in specific retention or capture of the ^{64}Cu-bearing polymers in acidic tissues such as tumours, while capture was suppressed in the background normal tissue. More specifically, at different time points (t_1, t_2,… t_n), different regions of the tumour could be acidified below the pH threshold (6.9), as indicated by the green spots in the front images in Fig. 7. This transient acidotic signal in turn activates ^{64}Cu-UPS micelles circulating at the tumour site into polycationic unimers, which are irreversibly captured, leaving a stable imprint of polymer signal (red spots on the positron map). The irreversible capture resulted in increased dose accumulation over time for ^{64}Cu-UPS, as validated experimentally (Supplementary Fig. 6). Furthermore, uptake of polymers inside the lysosomes of cancer cells avoids diffusion-caused signal blurring, which may explain the sharp contrast at the tumour and normal tissue boundary even after 24 h. Intact micelles are cleared from the tumour sites, as well as normal tissues through blood circulation. ^{64}Cu-UPS, by linking the binary activation in response to pH to a novel tissue retention output, suppresses the background while allowing maximum amplification of the tumour signal as approximated by 1 (tumour) or 0 (muscle/brain) outputs.

The data showed that ^{64}Cu-UPS tracers were able to detect a broad range of occult cancer types (Figs. 5 and 6) in the brain, head and neck, where FDG imaging is obscured by the high signal found in normal brain and tonsil tissues. Moreover, in a non-cancerous, LPS-induced inflammation model, FDG showed significantly increased uptake at LPS-injected muscle sites compared with the normal muscle control, whereas ^{64}Cu-UPS tracers showed insignificant increases (Fig. 4). For tumour imaging, although respectable dose accumulation of FDG was observed in tumours (for example, 5.4 ± 0.7%ID g^{-1} in HN5 tumours), high physiological uptake of FDG in healthy tissues hampers cancer-specific detection of tumours. A similar outcome was also observed in small molecular tracer MET for brain tumour detection, where high normal brain signals lowered tumour contrast compared with ^{64}Cu-UPS (Fig. 5 and Supplementary Fig. 9). For ^{64}Cu-UPS, coupling the unique binary output of phase transition to the capture of the acidotic signal allows a more cancer-specific detection of occult diseases (Fig. 6; see also three-dimensional (3D) rotation Supplementary Videos 1–3). Besides tumour acidosis, other factors, such as leaky tumour vasculature, disrupted blood–brain barriers (as in the case for 73C glioma), elevated micropinocytosis and impaired lymphatics may also contribute to the robust contrast of tumours over surrounding normal tissues by ^{64}Cu-UPS. Meanwhile, high uptake of ^{64}Cu-UPS in the reticuloendothelial systems (for example,he liver and spleen) may preclude the use of this agent for the detection of cancers in these organs.

In summary, we report the molecular mechanism of proton transistor-like nanoparticles to capture and integrate tumour acidotic signals into discrete outputs to improve the precision of cancer detection. This represents a second output—tissue retention—coupled to the transistor-like binary behaviour of the UPS nanoparticles besides fluorescence readout. The impact of the concept is illustrated by the non-invasive detection of small occult diseases (10–20 mm^3 or 3–4 mm) in the brain, head/neck and breast by PET imaging. Incorporation of both PET and fluorescence functions in one UPS nanotracer further synergizes two orthogonal imaging modalities, which potentially allows initial whole-body assessment of tumour burden by PET, followed by high-resolution fluorescence imaging for local interventions (for example, biopsy or surgery). We anticipate that the proposed chemical integration mechanism will impact early cancer detection and surveillance while creating strategic insights to incorporate molecular cooperativity principles[45] for the design of precision medicine.

Methods

Synthesis of ICG- and NOTA-conjugated UPS$_{6.9}$ nanoprobes and NOTA-PEG-*b*-PLA nanoparticles. The PEG-*b*-PEPA copolymer was synthesized following the reported procedure using the atom transfer radical polymerization method[24]. The polymers were then dissolved in methanol. ICG-Sulfo-OSu was first added to react with the amino group (1:1 molar ratio) via *N*-hydroxysuccinimide ester chemistry[46] for 1 h. Next, p-SCN-Bn-NOTA was added to react with the remaining amino group (4:1 molar ratio) overnight at room temperature. Unconjugated ICG and NOTA were removed using Millipore ultrafiltration membranes with a molecular weight cutoff of 10 kDa. The UPS$_{6.9}$ nanoprobes were produced via a solvent evaporation method[47], and concentrated to 5 mg ml^{-1} for further use.

NOTA-conjugated PEG-*b*-PLA block copolymers were synthesized by ring-opening polymerization following a published procedure[48]. Briefly, polymerization of D,L-lactide was performed at 110 °C using Fmoc-amine-PEG5K-hydroxyl as the macroinitiator and Sn(Oct)$_2$ as a catalyst. Deprotection of Fmoc was achieved by 20% piperidine in dimethylformamide. After polymer purification with precipitation in ether three times, the solid polymer was suspended in dimethylformamide and reacted with p-SCN-Bn-NOTA at room temperature overnight. Unconjugated NOTA was removed using Millipore ultrafiltration membranes with a molecular weight cutoff of 10 kDa.

^{64}Cu labelling of UPS$_{6.9}$ or PEG-*b*-PLA nanoprobes. Chelation of ^{64}Cu^{2+} to NOTA on the UPS$_{6.9}$ or PEG-*b*-PLA copolymer was accomplished by adjusting the pH to 6.0–6.5 with 4 M ammonium acetate buffer for 15 min at 37 °C. Micelle formation was carried out by adjusting the solution pH to 7.4 with 2 M sodium carbonate. Removal of unbound ^{64}CuCl$_2$ was achieved by centrifugal membrane filtration with a molecular weight cutoff of 100 kD three times. The maximum specific activity of the ^{64}Cu-UPS nanosensor is 1,860 Ci mmol^{-1}. Before and after centrifugal filtration, 1 µl of micelle solution was mixed with 8 µl deionized water and 1 µl 50 mM diethylenetriamine pentaacetate for 5 min. A 2 µl mixture was then spotted on a TLC plate and eluted with the mobile phase (PBS). The labelling efficiency was determined by radio-TLC.

pH titration and dialysis. UPS$_{6.9}$ polymers were first dissolved in 2.5 ml 0.1 M HCl and diluted to 2.0 mg ml^{-1} with deionized water. Sodium chloride was added to adjust the salt concentration to 150 mM. pH titration was performed by adding small volumes (1 µl in increments) of 4.0 M NaOH solution under stirring. The pH increase in the range of 3–11 was monitored as a function of the total added volume of NaOH. The fully protonated and complete deprotonation states (that is, where the protonation degree equalled 100 and 0%, respectively) were determined by the two extreme-value points of first-derivation pH titration curves. The pH values were measured using a Mettler Toledo pH meter with a microelectrode. Next, UPS$_{6.9}$ polymers with a protonation degree of 50% were obtained by adding corresponding volumes of 4.0 M NaOH. Then, 10 ml of polymer solution was centrifuged using an ultracentrifugation tube with a molecular weight cutoff of 100 kDa, to produce ~5 ml of filtrated sample. pH titrations were performed to quantify the amount of polymers and the degree of protonation in both residual and filtrate layers. We repeated the experiments three times and present the results as means ± s.d.

Cell culture. The cancer cell lines used for the in vivo tumour models included HN5, FaDu, human head and neck cancers, 4T1 breast cancers, and GFP-labelled glioma cells with *p53*$^{-/-}$, *PTEN*$^{-/-}$ and *BRAF*^{V600E} mutation (also known as 73C glioma cells). The HN5 and FaDu cell lines were obtained from the laboratory of M. Story; the 4T1 cell line was obtained from the laboratory of D. Boothman; and the 73C glioma cells were originally obtained from the laboratory of R. Bachoo at the University of Texas Southwestern. All cells lines were tested for mycoplasma contamination before use. Negative status for contamination was verified using a Mycoplasma Detection Kit from Biotool. Cells were cultured in DMEM or RPMI medium with 10% foetal bovine serum and antibiotics.

Animal models. Animal protocols related to this study were reviewed and approved by the Institutional Animal Care and Use Committee. Female non-obese diabetic and severe combined immunodeficient mice (6–8 weeks of age; ~20 g) were purchased from the University of Texas Southwestern Medical Center Breeding Core. For orthotopic head and neck tumours, HN5 and FaDu (2×10^6 mouse^{-1}) were injected into the submental triangle area. One week after inoculation, animals with a tumour size of 20–100 mm^3 were used for imaging studies. The orthotopic murine 4T1 breast tumour model was established in female BALB/c mice (6–8 weeks of age, ~20 g) by injection of 4T1 cells (5×10^5 mouse^{-1}) into the mammary fat pads. The GFP-transfected 73C murine glioma model was established by implanting 10^4 glioma cells intracranially into the striatum (2 mm, 0.5 mm, −2.5 mm; coordinates to the location of tumour cells with respect to the original point at the bregma) of the right hemisphere in male C57BL/6J mice (6–8 weeks of age; ~20 g). Gliomas (2–4 mm in diameter) were formed within 2–3 weeks in mice. The LPS-induced inflammation animal models were established by subcutaneous injection of 50 μg per 20 μl LPS into the right hind leg of BALB/c mice 2 d before the imaging. As a control, 20 μl PBS was injected subcutaneously into the left hind leg of the same mice.

Cell uptake assay. Some 1.5×10^4 HN5 cancer cells were seeded into individual wells of 96-well plates ($n=3$ for each time point) containing 0.2 ml DMEM media overnight before the nanoprobe incubation. Then, 20 μg ml^{-1} ^{64}Cu-$UPS_{6.9}$ or ^{64}Cu-PEG-PLA dispersed in either pH 6.5 or pH 7.4 DMEM medium containing 40 mg ml^{-1} HSA were incubated with HN5 cells. At a specific time point, the cell wells were washed with cold PBS buffer three times to remove all of the non-trapped nanoprobes. Finally, the 96-well plates were exposed on Perkin Elmer storage phosphor screens overnight, then imaged using Typhoon imager for ^{64}Cu tracer quantification. For confocal imaging, after nanoprobe incubation, the cells were fixed with 4% paraformaldehyde in PBS for 10 min at room temperature, and permeabilized with 0.1% Triton X-100 in PBS for 10 min at 4 °C. Cells were then stained with Hoechst 33342, anti-F-actin and anti-lysosomal-associated membrane protein 1 for nucleus, cell membrane and lysosomes, respectively. Anti-poly(ethylene glycol) antibody was used to label the $UPS_{6.9}$ copolymer.

In vivo PET/computed tomography imaging. For ^{64}Cu-$UPS_{6.9}$, mice received ~100 μCi of nanoprobes in 150 μl saline intravenously via tail vein injection. PET/computed tomography images were acquired 18–24 h postinjection on a Siemens Inveon PET/CT Multi-Modality System for 15 min. For the FDG experiment, mice were fasted for 12 h before PET imaging. Each mouse received 150 μCi FDG in 150 μl saline intravenously via tail vein injection. PET/computed tomography images were acquired 1 h postinjection for 15 min. The mice were sedated on the imaging bed under 2% isoflurane for the duration of imaging. Immediately after the computed tomography data acquisition (performed at 80 kV and 500 μA with a focal spot of 58 μm), 15-min static PET scans were conducted. The PET images were reconstructed using a Fourier rebinning and ordered subsets expectation maximization 3D algorithm. Reconstructed computed tomography and PET images were fused and analysed using Inveon Research Workplace software. PET images were then reconstructed into a single frame using the 3D ordered subsets expectation maximization/maximum a posteriori algorithm. Regions of interest were drawn manually as guided by computed tomography encompassing the tumour in all planes containing the tissue. The target activity was quantitatively calculated as %ID g^{-1}. The CNR was calculated as[49,50]:

$$\mathrm{CNR}=\frac{\text{mean activity (tumour)}-\text{mean activity (background)}}{\text{s.d. (background)}}$$

The background signal was measured as the mean activity in the surrounding normal muscle tissues, with the exception of 73C brain tumours. For 73C gliomas, the background signal was measured from the contralateral normal brain tissues. s.d. (background) refers to the standard deviation of the background tissues. The TBR was calculated as mean activity (tumour)/mean activity (background).

Ex vivo autoradiography and histology. Immediately following PET imaging, the mice were sacrificed, and the tumour and major organs (for example, brain, liver, spleen, heart, kidney, muscle, and so on) were harvested and frozen. Section slides were prepared from each specimen. The slides were first exposed on Perkin Elmer storage phosphor screens, then imaged using Typhoon imager for ^{64}Cu tracer quantification, followed by fluorescence imaging using a LI-COR Odyssey flatbed scanner with an 800 nm filter for the ICG signal. Finally, haematoxylin and eosin staining was performed for histological correlation of the tumours.

Statistical analysis. Data are expressed as means ± s.d. Sample sizes were chosen to ensure adequate power (>85% at a significance level of $P<0.05$) to detect predicted effect sizes, and were estimated on the basis of either preliminary data or previous experiences with similar experiments. Differences between groups were assessed using GraphPad Prism 8, with paired or unpaired two-sided Student's *t*-tests for the calculation of *P* values.

Reporting summary. Further information on research design is available in the Nature Research Reporting Summary linked to this article.

Data availability

The authors declare that the main data supporting the results in this study are available within the paper and its Supplementary Information. The raw and analysed datasets generated during the study are available for research purposes from the corresponding authors on reasonable request.

Received: 28 August 2018; Accepted: 13 May 2019;
Published online: 24 June 2019

References

1. Vogelstein, B. et al. Cancer genome landscapes. *Science* **339**, 1546–1558 (2013).
2. Jacobs, T. W., Gown, A. M., Yaziji, H., Barnes, M. J. & Schnitt, S. J. HER-2/neu protein expression in breast cancer evaluated by immunohistochemistry. A study of interlaboratory agreement. *Am. J. Clin. Pathol.* **113**, 251–258 (2000).
3. Paik, S. et al. HER2 and choice of adjuvant chemotherapy for invasive breast cancer: National Surgical Adjuvant Breast and Bowel Project Protocol B-15. *J. Natl Cancer Inst.* **92**, 1991–1998 (2000).
4. Hanahan, D. & Weinberg, R. A. Hallmarks of cancer: the next generation. *Cell* **144**, 646–674 (2011).
5. Heiden, M. G. V., Cantley, L. C. & Thompson, C. B. Understanding the Warburg effect: the metabolic requirements of cell proliferation. *Science* **324**, 1029–1033 (2009).
6. Hensley, C. T. et al. Metabolic heterogeneity in human lung tumours. *Cell* **164**, 681–694 (2016).
7. Zhu, A., Lee, D. & Shim, H. Metabolic positron emission tomography imaging in cancer detection and therapy response. *Semin. Oncol.* **38**, 55–69 (2011).
8. Som, P. et al. A fluorinated glucose analog, 2-fluoro-2-deoxy-D-glucose (F-18): nontoxic tracer for rapid tumour detection. *J. Nucl. Med.* **21**, 670–675 (1980).
9. Cook, G. J., Wegner, E. A. & Fogelman, I. Pitfalls and artifacts in ^{18}FDG PET and PET/CT oncologic imaging. *Semin. Nucl. Med.* **34**, 122–133 (2004).
10. Purohit, B. S. et al. FDG-PET/CT pitfalls in oncological head and neck imaging. *Insights Imaging* **5**, 585–602 (2014).
11. Truong, M. T., Viswanathan, C., Carter, B. W., Mawlawi, O. & Marom, E. M. PET/CT in the thorax: pitfalls. *Radiol. Clin. North Am.* **52**, 17–25 (2014).
12. Culverwell, A. D., Scarsbrook, A. F. & Chowdhury, F. U. False-positive uptake on 2-[^{18}F]-fluoro-2-deoxy-D-glucose (FDG) positron-emission tomography/computed tomography (PET/CT) in oncological imaging. *Clin. Radiol.* **66**, 366–382 (2011).
13. Truong, M. T. et al. Integrated positron emission tomography/computed tomography in patients with non-small cell lung cancer: normal variants and pitfalls. *J. Comput. Assist. Tomogr.* **29**, 205–209 (2005).
14. Bhargava, P., Rahman, S. & Wendt, J. Atlas of confounding factors in head and neck PET/CT imaging. *Clin. Nucl. Med.* **36**, e20–e29 (2011).
15. Blodgett, T. M., Mehta, A. S., Laymon, C. M., Carney, J. & Townsend, D. W. PET/CT artifacts. *Clin. Imaging* **35**, 49–63 (2011).
16. Fukui, M. B. et al. Combined PET-CT in the head and neck: part 2. Diagnostic uses and pitfalls of oncologic imaging. *Radiographics* **25**, 913–930 (2005).
17. Cohade, C., Mourtzikos, K. A. & Wahl, R. L. "USA-Fat": prevalence is related to ambient outdoor temperature—evaluation with ^{18}F-FDG PET/CT. *J. Nucl. Med.* **44**, 1267–1270 (2003).
18. Perkins, A. C., Mshelia, D. S., Symonds, M. E. & Sathekge, M. Prevalence and pattern of brown adipose tissue distribution of ^{18}F-FDG in patients undergoing PET-CT in a subtropical climatic zone. *Nucl. Med. Commun.* **34**, 168–174 (2013).
19. Gould, M. K., Maclean, C. C., Kuschner, W. G., Rydzak, C. E. & Owens, D. K. Accuracy of positron emission tomography for diagnosis of pulmonary nodules and mass lesions: a meta-analysis. *J. Am. Med. Assoc.* **285**, 914–924 (2001).
20. Harvey, R. J. et al. PET/CT in the assessment of previously treated skull base malignancies. *Head Neck* **32**, 76–84 (2010).
21. Schoder, H. in *Nuclear Oncology: Pathophysiology and Clinical Applications* (eds Strauss, H. W., Mariani, G., Volterrani, D. & Larson, S. M.) 269–295 (Springer, 2013).
22. Castaigne, C., Muylle, K. & Flamen, P. in *Head and Neck Cancer Imaging* (ed. Hermans, R.) 329–343 (Springer, 2006).
23. Schmalfuss, I. in *Head and Neck Cancer Imaging* (ed. Hermans, R.) 363–385 (Springer, 2012).
24. Zhao, T. et al. A transistor-like pH nanoprobe for tumour detection and image-guided surgery. *Nat. Biomed. Eng.* **1**, 0006 (2016).

25. Tsarevsky, N. V. & Matyjaszewski, K. "Green" atom transfer radical polymerization: from process design to preparation of well-defined environmentally friendly polymeric materials. *Chem. Rev.* **107**, 2270–2299 (2007).
26. Lopez-Fontal, E., Milanesi, L. & Tomas, S. Multivalence cooperativity leading to "all-or-nothing" assembly: the case of nucleation-growth in supramolecular polymers. *Chem. Sci.* **7**, 4468–4475 (2016).
27. Williamson, J. R. Cooperativity in macromolecular assembly. *Nat. Chem. Biol.* **4**, 458–465 (2008).
28. Moghimi, S. M. & Szebeni, J. Stealth liposomes and long circulating nanoparticles: critical issues in pharmacokinetics, opsonization and protein-binding properties. *Prog. Lipid Res.* **42**, 463–478 (2003).
29. Hess, S., Hansson, S. H., Pedersen, K. T., Basu, S. & Hoilund-Carlsen, P. F. FDG-PET/CT in infectious and inflammatory diseases. *PET Clin.* **9**, 497–519 (2014).
30. Wen, P. Y. & Kesari, S. Malignant gliomas in adults. *N. Engl. J. Med.* **359**, 492–507 (2008).
31. Omuro, A. & DeAngelis, L. M. Glioblastoma and other malignant gliomas: a clinical review. *J. Am. Med. Assoc.* **310**, 1842–1850 (2013).
32. Fink, J. R., Muzi, M., Peck, M. & Krohn, K. A. Multimodality brain tumor imaging: MR imaging, PET, and PET/MR Imaging. *J. Nucl. Med.* **56**, 1554–1561 (2015).
33. Becherer, A. et al. Brain tumour imaging with PET: a comparison between [^{18}F]fluorodopa and [^{11}C]methionine. *Eur. J. Nucl. Med. Mol. Imaging* **30**, 1561–1567 (2003).
34. Glaudemans, A. W. et al. Value of ^{11}C-methionine PET in imaging brain tumours and metastases. *Eur. J. Nucl. Med. Mol. Imaging* **40**, 615–635 (2013).
35. Juhasz, C., Dwivedi, S., Kamson, D. O., Michelhaugh, S. K. & Mittal, S. Comparison of amino acid positron emission tomographic radiotracers for molecular imaging of primary and metastatic brain tumours. *Mol. Imaging* **13**, 1–16 (2014).
36. Harris, R. J. et al. pH-weighted molecular imaging of gliomas using amine chemical exchange saturation transfer MRI. *Neuro-Oncol.* **17**, 1514–1524 (2015).
37. Thews, O. et al. Activation of P-glycoprotein (Pgp)-mediated drug efflux by extracellular acidosis: in vivo imaging with ^{68}Ga-labelled PET tracer. *Eur. J. Nucl. Med. Mol. Imaging* **37**, 1935–1942 (2010).
38. Demoin, D. W. et al. PET imaging of extracellular pH in tumours with ^{64}Cu- and ^{18}F-labeled pHLIP peptides: a structure–activity optimization study. *Bioconjug. Chem.* **27**, 2014–2023 (2016).
39. Vavere, A. L. et al. A novel technology for the imaging of acidic prostate tumours by positron emission tomography. *Cancer Res.* **69**, 4510–4516 (2009).
40. Weerakkody, D. et al. Family of pH (low) insertion peptides for tumour targeting. *Proc. Natl Acad. Sci. USA* **110**, 5834–5839 (2013).
41. Urano, Y. et al. Selective molecular imaging of viable cancer cells with pH-activatable fluorescence probes. *Nat. Med.* **15**, 104–109 (2009).
42. Gillies, R. J., Liu, Z. & Bhujwalla, Z. P-31-Mrs measurements of extracellular Ph of tumours using 3-aminopropylphosphonate. *Am. J. Physiol.* **267**, C195–C203 (1994).
43. Gillies, R. J., Raghunand, N., Garcia-Martin, M. L. & Gatenby, R. A. PH imaging. *IEEE Eng. Med. Biol. Mag.* **23**, 57–64 (2004).
44. Volk, T., Jahde, E., Fortmeyer, H. P., Glusenkamp, K. H. & Rajewsky, M. F. pH in human tumour xenografts: effect of intravenous administration of glucose. *Br. J. Cancer* **68**, 492–500 (1993).
45. Li, Y., Wang, Y., Huang, G. & Gao, J. Cooperativity principles in self-assembled nanomedicine. *Chem. Rev.* **118**, 5359–5391 (2018).
46. Ma, X. et al. Ultra-pH-sensitive nanoprobe library with broad pH tunability and fluorescence emissions. *J. Am. Chem. Soc.* **136**, 11085–11092 (2014).
47. Wang, Y. et al. A nanoparticle-based strategy for the imaging of a broad range of tumours by nonlinear amplification of microenvironment signals. *Nat. Mater.* **13**, 204–212 (2014).
48. Blanco, E. et al. β-lapachone micellar nanotherapeutics for non-small cell lung cancer therapy. *Cancer Res.* **70**, 3896–3904 (2010).
49. Fin, L., Bailly, P., Daouk, J. & Meyer, M. E. A practical way to improve contrast-to-noise ratio and quantitation for statistical-based iterative reconstruction in whole-body PET imaging. *Med. Phys.* **36**, 3072–3079 (2009).
50. Yan, J., Schaefferkoette, J., Conti, M. & Townsend, D. A method to assess image quality for low-dose PET: analysis of SNR, CNR, bias and image noise. *Cancer Imaging* **16**, 26 (2016).

Acknowledgements

We thank R. Bachoo for the original 73C cancer cells, Y. Li and Q. Feng for helpful discussions. This work is supported by the National Institutes of Health (R01CA192221 and R01CA211930) and Cancer Prevention and Research Institute of Texas (RP180343). The animal imaging work was supported by a University of Texas Southwestern Small Animal Imaging Resource Grant (U24 CA126608), and radiochemistry and PET imaging were supported by a Simmons Cancer Center Support Grant (P30 CA142543) and CPRIT Grant (RP110771) to X.S.

Author contributions

G.Huang, B.D.S. and J.G. are responsible for all of the phases of the research. G.Huang performed all of the experiments and analyses. T.Z. assisted the polymer synthesis and FDG-PET imaging. C.W. performed the confocal imaging on cell uptake of nanoprobes. K.N. ran the PET/CT scan and imaging analysis. Y.X. performed the initial radiolabelling experiments. X.G. and Y.W. prepared the 73C brain tumour model. G.Hao helped with ^{64}Cu coupling with UPS nanoprobes. W.-P.G. assisted with the analysis of the 73C brain tumour study. X.S. helped design the FDG and ^{64}Cu PET experiments.

Competing interests

B.D.S. and J.G. are scientific co-founders and scientific advisors of OncoNano Medicine, Inc. G.Huang is a scientific advisor for OncoNano Medicine, Inc. T.Z. is currently an employee of OncoNano Medicine, Inc.

Additional information

Supplementary information is available for this paper at https://doi.org/10.1038/s41551-019-0416-1.

Reprints and permissions information is available at www.nature.com/reprints.

Correspondence and requests for materials should be addressed to B.D.S. or J.G.

Publisher's note: Springer Nature remains neutral with regard to jurisdictional claims in published maps and institutional affiliations.

nature research

Corresponding author(s): Jinming Gao, Baran D. Sumer

Last updated by author(s): May 10, 2019

Reporting Summary

Nature Research wishes to improve the reproducibility of the work that we publish. This form provides structure for consistency and transparency in reporting. For further information on Nature Research policies, see Authors & Referees and the Editorial Policy Checklist.

Statistics

For all statistical analyses, confirm that the following items are present in the figure legend, table legend, main text, or Methods section.

n/a	Confirmed	
☐	☒	The exact sample size (*n*) for each experimental group/condition, given as a discrete number and unit of measurement
☐	☒	A statement on whether measurements were taken from distinct samples or whether the same sample was measured repeatedly
☐	☒	The statistical test(s) used AND whether they are one- or two-sided *Only common tests should be described solely by name; describe more complex techniques in the Methods section.*
☒	☐	A description of all covariates tested
☒	☐	A description of any assumptions or corrections, such as tests of normality and adjustment for multiple comparisons
☐	☒	A full description of the statistical parameters including central tendency (e.g. means) or other basic estimates (e.g. regression coefficient) AND variation (e.g. standard deviation) or associated estimates of uncertainty (e.g. confidence intervals)
☒	☐	For null hypothesis testing, the test statistic (e.g. *F*, *t*, *r*) with confidence intervals, effect sizes, degrees of freedom and *P* value noted *Give P values as exact values whenever suitable.*
☒	☐	For Bayesian analysis, information on the choice of priors and Markov chain Monte Carlo settings
☒	☐	For hierarchical and complex designs, identification of the appropriate level for tests and full reporting of outcomes
☒	☐	Estimates of effect sizes (e.g. Cohen's *d*, Pearson's *r*), indicating how they were calculated

Our web collection on statistics for biologists contains articles on many of the points above.

Software and code

Policy information about availability of computer code

Data collection	The PET images were reconstructed by using a Fourier Rebinning and Ordered Subsets Expectation Maximization 3D (OSEM3D) algorithm. Regions of interest (ROI) were drawn manually as guided by CT encompassing the tumour in all planes containing the tissue. The target activity was quantitatively calculated as percentage injected dose per gram of tissue (%ID/g). The contrast-to-noise ratio was calculated as (tumour mean activity – background mean activity) / background standard deviation.
Data analysis	PET signal quantification was analysed using Inveon Research Workplace (IRW) software. Statistical analyses were performed by GraphPad Prism 8 using paired or unpaired, two-sided Student's t-tests for the calculation of p-values.

For manuscripts utilizing custom algorithms or software that are central to the research but not yet described in published literature, software must be made available to editors/reviewers. We strongly encourage code deposition in a community repository (e.g. GitHub). See the Nature Research guidelines for submitting code & software for further information.

Data

Policy information about availability of data

All manuscripts must include a data availability statement. This statement should provide the following information, where applicable:

- Accession codes, unique identifiers, or web links for publicly available datasets
- A list of figures that have associated raw data
- A description of any restrictions on data availability

The authors declare that the main data supporting the results in this study are available within the paper and its Supplementary Information. The raw and analysed datasets generated during the study are available for research purposes from the corresponding authors on reasonable request.

Field-specific reporting

Please select the one below that is the best fit for your research. If you are not sure, read the appropriate sections before making your selection.

☒ Life sciences ☐ Behavioural & social sciences ☐ Ecological, evolutionary & environmental sciences

For a reference copy of the document with all sections, see nature.com/documents/nr-reporting-summary-flat.pdf

Life sciences study design

All studies must disclose on these points even when the disclosure is negative.

Sample size	Sample sizes were chosen to ensure adequate power (>85%, at significance of 0.05) to detect predicted effect sizes, which were estimated on the basis of either preliminary data or previous experiences with similar experiments.
Data exclusions	No data were excluded.
Replication	All attempts at replication are successful.
Randomization	The animals were randomized by independent technician without knowing the group assignment.
Blinding	The technician carried out the data collection and analysis without knowing the group assignment for each sample.

Reporting for specific materials, systems and methods

We require information from authors about some types of materials, experimental systems and methods used in many studies. Here, indicate whether each material, system or method listed is relevant to your study. If you are not sure if a list item applies to your research, read the appropriate section before selecting a response.

Materials & experimental systems

n/a	Involved in the study
☐	☒ Antibodies
☐	☒ Eukaryotic cell lines
☒	☐ Palaeontology
☐	☒ Animals and other organisms
☒	☐ Human research participants
☒	☐ Clinical data

Methods

n/a	Involved in the study
☒	☐ ChIP-seq
☒	☐ Flow cytometry
☒	☐ MRI-based neuroimaging

Antibodies

Antibodies used	Anti-poly(ethylene glycol) antibody (ab190652), anti-F-actin, anti-LAMP1 and anti-GLUT1 were all purchased from abcam. Hoechst 33342 (Invitrogen).
Validation	Validation of each antibody was done under standard information offered by the supplier.

Eukaryotic cell lines

Policy information about cell lines

Cell line source(s)	HN5 and FaDu cell lines were obtained from Michael Story's lab; 4T1 were obtained from David Boothman lab; 73C glioma cells were originally obtained from Robert Bachoo lab at UT Southwestern.
Authentication	None of the cell lines used were authenticated.
Mycoplasma contamination	All cells lines were tested for mycoplasma contamination before use. Negative status for contamination was verified by Mycoplasma Detection Kit from Biotool. Cells were cultured in DMEM with 10% fetal bovine serum and antibiotics.
Commonly misidentified lines (See ICLAC register)	No commonly misidentified lines were used in this study.

Animals and other organisms

Policy information about studies involving animals; ARRIVE guidelines recommended for reporting animal research

Laboratory animals	Female NOD-SCID mice (6–8 weeks, ~20 g), female BALB/c mice (6–8 weeks, 20 g) and male C57BL/6J mice (6–8 weeks, 20 g) were all purchased from UT Southwestern Medical Center Breeding Core.
Wild animals	The study did not involve wild animals.
Field-collected samples	The study did not involve samples collected from the field.
Ethics oversight	Animal protocols related to this study were reviewed and approved by the Institutional Animal Care and Use Committee.

Note that full information on the approval of the study protocol must also be provided in the manuscript.